Nonlinear oxidation kinetics of nickel cermets

Henning Galinski [*], Anja Bieberle-Hütter, Jennifer L.M. Rupp, Ludwig J. Gauckler

Nonmetallic Inorganic Materials, ETH Zurich, Zurich, Switzerland

Abstract

The oxidation of a cermet of screen-printed nickel (Ni) and gadolinia-doped ceria (CGO) with an approximate median porosity of 50 vol.% has been studied via in situ X-ray diffraction and focused ion beam nanotomography in the temperature range 773–848 K. The oxidation kinetics of Ni to NiO is found to be highly nonlinear with an apparent activation energy of 2.8(2) eV in this temperature range. The nonlinear oxidation kinetics found is in good agreement with theoretical works on oxide growth driven by nonlinear inbuilt fields. Stress-induced Kirkendall void formation has been identified as the physical process that enhances the oxidation of Ni/CGO cermets. Compressive stresses within the Ni matrix result from the thermal expansion mismatch of Ni and CGO and cause plastic deformation as they exceed the yield stress of the Ni matrix. The pore size distribution of Kirkendall voids formed has been measured by FIB nanotomography and shows a significant temperature dependence. It is shown that even one cycle of reoxidation changes irreversibly the microstructure of the cermet which can be interpreted as the onset and main contribution to the mechanical degradation of the cermet.
© 2011 Acta Materialia Inc. Published by Elsevier Ltd. All rights reserved.

Keywords: Cermets; Kirkendall effect; Nonlinear kinetics; Nickel; Oxidation

1. Introduction

Porous metal ceramic composites, so-called "cermets", have drawn increasing attention in recent years [1]. Due in particular to their novel transport [2–6], mechanical [7], magnetic [8], catalytical [9] and optical properties [10], this class of inhomogeneous materials is already used in a wide range of applications. A cermet is typically composed of a three-dimensional metal network near the percolation threshold which is embedded in a 3-D percolating ceramic matrix. The physical properties of the cermet can therefore be controlled by the volume content of the two phases. In the case that cermets are used as catalysts, e.g. in solid oxide fuel cells (SOFCs), a third percolating porous phase is needed to guarantee continuous gas transport. Due to the complex interactions between the different phases, it is difficult to predict the physical properties of cermets by simulations.

Nickel (Ni)/yttrium-stabilized zirconia (YSZ) or Ni/ceria gadolinium oxide (CGO) cermets are "state of the art" anodes for high-temperature SOFCs. A necessary condition to run SOFCs is to maintain chemical and mechanical stability during fabrication, long-term operation and redox cycling [11]. Hence, redox cycling due to system-related shutdowns has become the current research focus as it has been found to have the most severe impact on the degradation of the SOFC anode [12–16]. A recent environmental transmission electron microscopy (ETEM) investigation of in situ reoxidation of Ni/YSZ cermets showed the formation of secondary pores during oxidation [17]. This effect has been related by Faes et al. to the reoxidation strain and the onset of plastic deformation in Ni/YSZ cermet [18].

In this paper, we address the oxidation kinetics and the related microstructural changes of a Ni/CGO cermet and compare it with the oxidation kinetics of pure Ni systems. The oxidation kinetics of metals is controlled by the coupled transport of ions and charge-compensating electrons and the evolving inbuilt electric field E during oxidation. The oxidation kinetics of Ni for different sample

---

* Corresponding author. Tel.: +41 446326061; Fax: +41 446321132.
  E-mail address: henning.galinski@mat.ethz.ch (H. Galinski).

geometries—bulk, particles, nanoparticles or thin films—has been the subject of research for decades. Except for Ni nanoparticles [19,20] and Ni particles embedded in an alumina matrix [20], the experimentally observed oxidation kinetics for Ni single crystals [21], Ni bulk [22] and Ni particles (>4.4 μm) [23,24] all follow a parabolic oxidation rate law. It has been found that NiO, which has a rock-salt structure, is a metal-deficient p-type semiconductor, the predominant defects being doubly ionized cation vacancies and electron holes.

However, the nonstoichiometry in this oxide is very low even at very high temperatures [25]. The growth process of the oxide shell on Ni at temperatures above 1273 K is governed by the outward diffusion of cations, and the participation of grain boundary diffusion in this reaction can be neglected. At temperatures below 1273 K, short-circuit diffusion along Ni vacancies in NiO grain boundaries is the dominant transport mechanism for the oxidation of Ni [26]. In several publications, it has been shown that nickel oxide modified with reactive elements such as Ce and Y has a lower oxidation rate than pure nickel oxide [27]. Czerwinski et al. have suggested that at high temperatures, >1000 K, the CeO$_2$ particles formed initially by oxidation of Ce additions dissolve, acting as a source of Ce^{4+} ions in NiO grain boundaries. It is believed that Ce^{4+} ion segregants impede the Ni^{2+} diffusion, while allowing O^{2-} diffusion to continue; this results in a change of oxide growth mechanism as compared to pure NiO [28].

2. Theory

Under steady-state conditions, the growth rate of an oxide film with thickness L is determined by the product of ionic particle density J_i at the metal–oxide interface and the volume of oxide R_i that is formed per arriving ionic species i at this interface:

$$\frac{dL_{\text{oxide}}(t)}{dt} = \sum_{i=1}^{N} R_i \cdot J_i. \tag{1}$$

Fromhold showed that once the electric field E inside the film during oxidation can be treated as homogeneous, the total potential ϕ across the growing film is no longer dependent on its thickness L [29]. As a consequence the total oxidation-rate driven by the nonlinear diffusion of electrons can be written as follows:

$$R_i \cdot J_i = \frac{L_{crit}}{t_{crit}} \sinh \left[\frac{L_{crit}}{L(t)} \right], \tag{2}$$

where L_{crit} is the critical oxide thickness that indicates the transition between linear and nonlinear diffusion and $t_{crit} = L_{crit}^2 / k_p$ is the critical time scale with the parabolic rate constant k_p. In the case of common diffusion of defects in oxides, k_p is represented by a standard Arrhenius ansatz:

$$k_p = k_0 \cdot \exp[-E_a / k_b T], \tag{3}$$

with k_0 representing the prefactor and E_a the activation energy necessary for jumps to adjacent defect sites. The functional form of Eq. 2 equals the one of the Mott–Cabrera equation [30]. For a detailed derivation of Eq. 2, the reader is referred to the fundamental work of Fromhold [31]. In the limit of very thin films, where space charges are negligible, and thick films, where local space charge neutrality is indicated, the ion and electron transport follows the linear diffusion equation:

$$J_i = -D_i \nabla c_i + \mu E c_i \tag{4}$$

and the oxide growth obeys a power law $L(t) \propto t^{\frac{1}{\beta}}$, which is a generalization of the known parabolic rate law with $\beta = 2$. Assuming a linear inbuilt field E, Carter [32] and Fromhold [31] extended the present theory to cope with nonplanar systems, e.g. spherical particles or spherical cavities. For nonplanar geometries, the overall oxidation rate is expressed in terms of the volume of oxide V_{oxide} formed per time step or the experimentally more suitable oxidation ratio $x(t)$. The time derivative of the oxidation ratio equals the integral of the ionic flux through the reactive interface divided by the product of the initial metal volume and the relative volume expansion factor σ. The time derivative reads:

$$\frac{dx_{\text{oxide}}(t)}{dt} = \frac{R_1 \int_{\text{Reaction Interface}} J_1 \, dA}{\sigma_{\text{Ni} \rightarrow \text{NiO}} \cdot V_{\text{metal}}} = \frac{R_1 \cdot I_1}{\sigma_{\text{Ni} \rightarrow \text{NiO}} \cdot V_{\text{metal}}}, \tag{5}$$

with the total ionic current I_1 contributing to the oxide growth and $\sigma_{\text{Ni} \rightarrow \text{NiO}} = 1.665$ [19]. The total ionic current I_1 depends on the time-dependent radius of the shrinking metal particle a and the growing oxide shell with radius b as shown in Fig. 1. Once the inbuilt field E exceeds $\approx 10^4 \text{V m}^{-1}$, the linear field approximation of Carter [32] and Fromhold [31] no longer holds and nonlinear effects have to be taken into account. For this case Niklasson [19] proposed—in analogy to the oxidation rate laws for planar systems—a solution for metallic nanoparticles:

$$R_1 \cdot I_1 = 4\pi k_p \left(\frac{a(x) \, b(x)}{L_{crit}} \right) \sinh \left[\frac{L_{crit}}{L(x)} \right]. \tag{6}$$

For a fixed initial value $x(t_0)$, Eqs. 5 and 6 can be solved by numerical integration. In contrast to common bulk metals or nanoparticles, a cermet is composed of two solid phases, which generally have different thermal expansion coefficients α. Hence, an complementary elastic strain
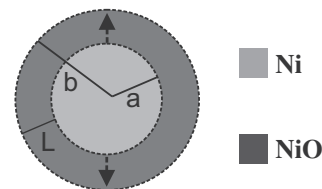
Fig. 1. Schematic illustration of the oxidation mechanism of a spherical Ni particle: (a) denotes the radius of the remaining Ni particle and (b) the radius of the formed NiO shell. The dominating outward diffusion of Ni is indicated by the black arrows.

energy μ_{elast} in the Ni network caused by compressive stresses is going to enhance the current density at the reaction interface $J_1 \propto \nabla \mu_{elast}$ [33]. This will contribute additively to the evolving inbuilt field E during oxidation.

3. Experimental

3.1. Sample preparation

In order to study the oxidation kinetics and its impact on the mechanical integrity of the oxidation kinetics of Ni/CGO cermets, NiO/CGO screenprinted on YSZ tape (Hexis AG, Switzerland) was annealed in a tube furnace under a reducing atmosphere (95%N_2, 5%H_2) at 1273 K for 2 h.

The oxidation kinetics of the Ni component of the Ni cermet was investigated by means of in situ X-ray diffraction. The studies were carried out at 773–848 K in air in a $\theta - 2\theta$ diffractometer using Cu Kα radiation (X-Pert PANalytical) equipped with a hot stage (Anton Paar HTK 1200N). The samples were subsequently embedded in epoxy cold mounting resin (Epofix Hardener, Struers) to infiltrate the porous structure of the cermet, avoiding difficulties during image analysis.

3.2. Oxidation kinetics

The oxidation kinetics is analyzed by measuring the intensity of the $Ni_{(111)}$-peak for five different oxidation temperatures T_{ox} in the range 773–848 K. The intensity of the $Ni_{(111)}$-peak decreases with time due to the transformation of Ni to NiO during heating. For any time the oxidation ratio $x(t)$ is given by:

$$x(t) = 1 - (I_{Ni}(t)/I_{Ni}(t_0)). \tag{7}$$

The measured oxidation ratios $x(t)$ where fitted with k_p as a free variable to the solution of Eqs. 5 and 6 using a least-squares approach.

3.3. Image acquisition

In order to match the requirements for reliable 2-D and 3-D data for the Ni/CGO cermet, it is essential to use focused ion beam (FIB) etching in combination with high-resolution electron microscopy (HREM) equipped with an energy- and angle-selective backscattering detector (EsB). Single and multiple cross-sections of the Ni/CGO were cut, polished and imaged using a Zeiss NVISION 40 FIB etching system. All samples are coated with carbon to preserve fine details and protect the sample from radiation damage by the Ga-ion beam. The stacks of multiple cross-sections were aligned recursively by Stackreg [34] and reconstructed using AVS Express. The resulting tomographic images comprised cubic voxels 11 nm in size. The size distribution of secondary pores (PSD) in NiO/CGO was calculated from the 3-D reconstructions using a self-written recursive C# 3-D particle analysis algorithm.

4. Results and discussion

4.1. Oxidation kinetics

The oxidation experiments were carried out on as-reduced Ni/CGO cermets. The composition and microstructure were analyzed by standard HREM on FIB cross-sections. In Fig. 2 a typical cross-section of a previously reduced Ni/CGO cermet is shown. EsB yields the grain orientation contrast in the Ni phase as well as the mean grain size of the Ni network, $d_{Ni} = 450(50)$ nm. The volume fractions of the three different phases are as follows: $\phi_{Ni} \approx 25\%$, $\phi_{CGO} \approx 25\%$ and $\phi_{pores} \approx 50\%$. All three phases are homogeneously distributed and show no sign of porosity or cracks. The oxidation ratio $x(t)$ has been determined as a function of time t for five different oxidation temperatures T_{ox} in the range 773–848 K by Eq. 7 and plotted in Fig. 3a. The functional shape of $x(t)$ is similar for all T_{ox} and deviates clearly from the oxidation rate profiles expected for linear field assisted ion diffusion [29] as denoted by the dotted curve in Fig. 3a. In comparison to the oxidation kinetics driven by a linear-field E, the oxidation kinetics of the experimental dataset obtained in this work is enhanced at shorter times. The oxidation kinetics found differs significantly from the common power growth laws $L(t) \propto t^{\frac{1}{\beta}}$, which are plotted on a log–log scale as straight lines with slopes β. The experimentally observed enhancement of the oxidation kinetics at the beginning of the oxidation is in good agreement with theoretical predictions for nonlinear oxidation kinetics given by Eqs. 5 and 6 as developed by Niklasson [19] for high inbuilt electric fields E. A least-squares approach has been used to fit the numerically integrated Eqs. 5 and 6 to the experimental data, whereby $L_{cr} = 10$ nm was kept constant and k_p and $x(t_0)$ were used as free fitting parameters. The best fits for Eq. 5 are shown in Fig. 3a as dotted lines. For all T_{ox}, a good agreement between the experimental data and the oxidation model has been achieved. The Debye length of stochiometric NiO at 773 K is, for $\lambda_d < 1$ μm, in the range of the Ni phase grain size $d_{Ni} = 450(50)$ nm [35]. Therefore,
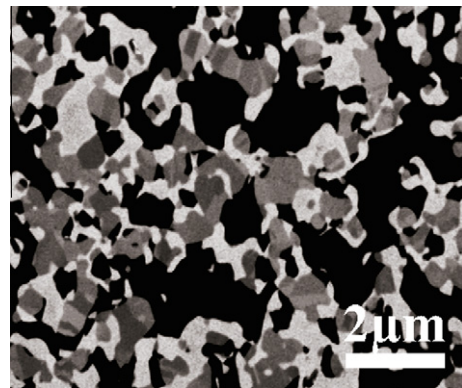
Fig. 2. FIB cross-section image of an as-reduced (95%N_2, 5%H_2, 1273 K, 2 h) screen-printed Ni/CGO cermet with Ni phase (grey)–CGO (white) and pores filled with epoxy resin (black).
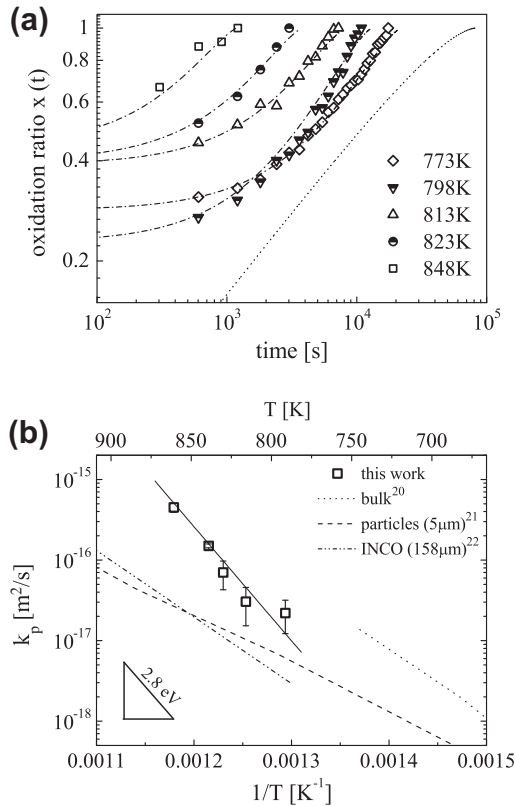
Fig. 3. (a) Experimentally observed oxidation ratios for different oxidation temperatures T as function of time t (symbols) fitted by Eqs. 5 and 6 representing a growth kinetics limited by nonlinear ion diffusion (dash-dotted). The dotted line denotes the equivalent shape of the oxidation ratio controlled by linear ion diffusion at 848 K. (b) Arrhenius plot of the derived parabolic oxidation rate constant k_p compared with data from the literature with different sample geometries (planar bulk, particles, commercial particles from INCO).

local space charge effects on the oxidation kinetics have to be taken into account.

The parabolic rate constant k_p derived from the best fits of Fig. 3a have been plotted in Fig. 3b as an Arrhenius diagram together with parabolic rate constants obtained from the literature for the oxidation of Ni bulk and Ni particles of various sizes. For all T_{ox}, k_p is in good agreement with the chosen Arrhenius approach in Eq. 3. The activation energy E_a for the diffusion process calculated from the slope is $E_a = 2.8(2)$ eV. Although the absolute values of k_p are comparable, the activation energy of $E_a = 2.8(2)$ eV found differs significantly from the literature data shown in Fig. 3b with 1.7 eV for the low-temperature oxidation of polycrystalline Ni [22] and 1.9–1.5 eV for the oxidation of Ni particles [19,36]. A high activation energy of 2.9 eV has also been reported for oxidation of polycrystalline Ni between 1148 and 1323 K by Gulbransen and has been related to failure of oxide–metal adhesion due to stress or oxygen dissolution [37]. Failure of oxide–metal adhesion implies that during and after oxidation the microstructural integrity is not longer conserved. In order to clarify the impact of stress and stress-induced microstructural changes

on the oxidation kinetics, the results of the measured thermal expansion of the Ni network and FIB cross-sectioning and nanotomography data of the cermet are presented in the next section.

4.2. Stress-induced Kirkendall voids

In contrast to pure materials, the oxidation of Ni in a cermet takes place in the vicinity of two other phases: the ceramic network and the pores. Hence, only the ceramic network is considered to impact the elastic strain energy of the Ni phase during oxidation. This is mostly due to the different thermal expansion coefficients of the two materials α_{Ni} [38] and α_{CGO} [39]. The corresponding compressive stress due to the thermal expansion mismatch in the Ni network reads:

$$\sigma = \frac{E_{Ni}}{1 - v_{Ni}} \cdot \Delta\alpha \Delta T, \tag{8}$$

where E_{Ni} is the Young's modulus, v_{Ni} the Poisson ratio and $\Delta\alpha = \alpha_{CGO} - \alpha_{Ni}$. The linear thermal expansion coefficient α of the Ni phase has been determined as function of temperature from the shifting Ni_{111}-peak during oxidation. The evolution of the lattice parameter a as function of T obeys a linear relation as a first approximation. Hence, the linear expansion coefficient of Ni in the cermet can be regarded as a constant in the small temperature range 773–848 K:

$$\alpha(T) = \frac{1}{a_0} \cdot \frac{da}{dT} = 12.7(7) \times 10^{-6} \text{ K}^{-1}, \tag{9}$$

where $a_0 = 0.3529$ represents the lattice parameter at room temperature. In Fig. 4a the experimentally determined values for α are compared to the literature data for the linear thermal expansion coefficient for Ni [38] and CGO [39], respectively. Neither obeys a linear relation as function of T and the thermal expansion coefficients α of the two materials differ over the entire temperature range by $\approx 3 \times 10^{-6}$ K. It becomes obvious that despite the large error margins, the Ni expansion in the cermet is suppressed during oxidation and in the range of the ceramic network. The impact of thermally generated vacancies on the thermal expansion coefficient [40] is, for a concentration of $c_V(848 \text{ K}) \approx 1^{-11}$, below the error margins of the measured thermal expansion coefficient α and can be disregarded. This result has been converted with Eq. 8 to the corresponding values of stress due to $\Delta\alpha$ and compared in Fig. 4b with the yield stress of commercial polycrystalline Ni with an average grain size of $d = 4.4$ μm [41]. The measured compressive stresses range between $\sigma_{773K} = 0.59(10)$ GPa and $\sigma_{848K} = 0.77(10)$ GPa. They are in accordance with the stress values obtained from the literature data [38,39].

It is remarkable that for all temperatures $T > 540$ K, and especially for the temperature range 773–848 K used in this work, the compressive stress $\sigma_{comp.}$ exceeds the yield stress σ_{Ni}^{yield}. Therefore it has to be expected that Ni in a Ni/CGO cermet undergoes plastic deformation once heated to
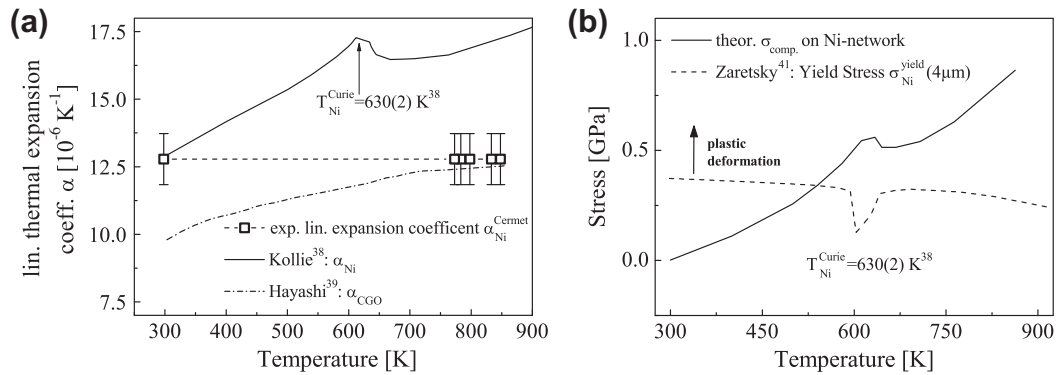
Fig. 4. (a) Measured linear thermal coefficient α in comparison to dilatometry data from the literature. The pronounced maximum of α_{Ni} around the Curie temperature is due to a magnetic phase transition. (b) The calculated compressive stress due to $\Delta\alpha$ in the Ni network in comparison to the yield stress of a commercially available polycrystalline Ni. The pronounced maximum of $\sigma_{comp.}$ and the minimum of σ_{Ni}^{yield} around the Curie temperature is due to a magnetic phase transition.

over $T > 540$ K. The onset of plastic deformation in combination with the local compressive stresses on the Ni network legitimate the assumption that the oxidation kinetics is severely impacted by this potential energy of elastic and plastic deformation. This result is in agreement with the findings of Faes et al. [18] on the oxidation of Ni/YSZ cermets. As consequence, the mismatch of the thermal expansion coefficients in the cermet is regarded as an additive contribution to the inbuilt electric field E that triggers the oxidation kinetics to be nonlinear. This effect is also mirrored in the microstructural changes during oxidation. Fig. 5 shows a Ni cermet after oxidation at 783 K; voids in the NiO phase have been formed during oxidation. This secondary porosity is located predominantly in the interior of the NiO grains. This microstructural feature indicates void formation as a result of the oxidation reaction Ni → NiO. The Ni oxidation kinetics as shown in Section 4.1 is nonlinear and especially at the beginning of the oxidation reaction characterized by a rapid outward diffusion of Ni cations through the oxide layer and inward diffusion by cation vacancies. As the stress acts only additively on the outward diffusion, the diffusion is unbalanced and leads to the observed condensation of vacancies [42] inside the Ni
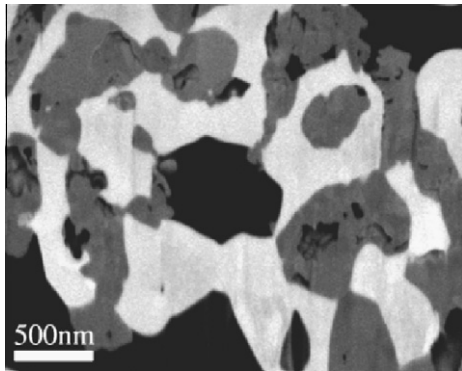
as seen in Fig. 5. Voids formed by the condensing vacancies are called Kirkendall voids and this phenomenon, which is also known from the degradation of solder joints, is called the Kirkendall effect [43,44].

Weinberg et al. [44] developed a general variational model for the growth of Kirkendall voids, including contributions from surface energy, thermal expansion mismatch, creep and diffusion. They showed that the vacancy concentration due to the unbalanced diffusion is a critical parameter, which determines whether a void formed in a metal matrix grows or anneals. A similar result has been found for different strain rates in the material, which act as damping parameter on the final void size.

In order to verify that the observed void condensation is due to the Kirkendall effect, FIB nanotomography has been used to reveal the pore size distribution function for two different oxidation temperatures. If the voids are formed due to the Kirkendall effect, the void-size distribution should shift due to the increased diffusion and stress to higher void radii for increasing oxidation temperatures. In Fig. 6a the 3-D reconstruction obtained from FIB nanotomography for a sample oxidized at 783 K is shown with two typically different void feature sizes corresponding to the pore network of the cermet and the condensed voids, respectively. The void-size distribution from the 3-D reconstruction has been determined by a recursive particle-tracking algorithm; the minimal size of a void was set to be two voxels (22 nm). The void-size distribution in Fig. 6b for oxidation temperatures of 783 and 848 K shows a significant temperature dependence. Hence, the formation of Kirkendall voids as well as the compressive stresses during oxidation increase the self-diffusion of the metal to the oxide–oxygen interface and contribute to the nonlinear oxidation kinetics of the Ni cermet. This result is in accordance with the in situ ETEM investigations of Jeangros et al., who found that secondary pores formed in the Ni phase during oxidation of a Ni/YSZ cermet [17].

The onset of the Kirkendall void formation can be defined by the critical temperature $T_{crit} \approx 540$ K where

Fig. 5. NiO (grey)/CGO (white) cermet, oxidized at *783* K. Primary pores (black) are filled with epoxy resin, secondary pores and cavities inside the NiO grains are visible.

(a)

pore

400³ nm³

(b)
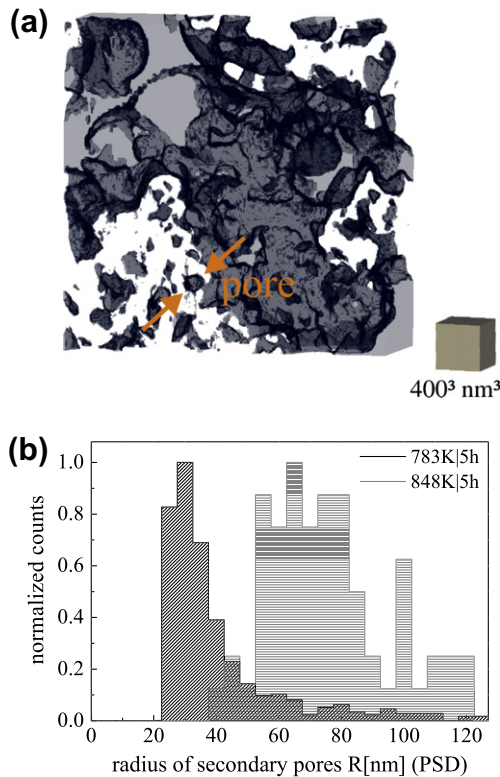
Fig. 6. (a) The 3-D reconstruction of the oxidized Ni cermet at 783 K indicating the formation of secondary pores. This formation of central cavities is known as the Kirkendall effect [43]. (b) The pore size distributions of two oxidized and analyzed samples show a significant temperature dependence.

the internal stresses σ_{Ni} exceed the yield stress σ_{Ni}^{yield} of the Ni matrix. With increasing T_{ox}, the center of the pore size distribution shifts to higher pore sizes due to the increasing grain boundary diffusion of Ni in NiO. It should be noted that this result applies only to situations where $T_{ox} <$ 1273 K. Once the diffusion mechanism during oxidation changes from grain boundary diffusion to volume diffusion at $T_{ox} \geqslant$ 1273 K, the response of the microstructure to oxidation will, without loss of generality, change as well.

5. Conclusion

In essence, it has been shown that the oxidation kinetics of a Ni cermet between 773 and 848 K is nonlinear and deviates from known parabolic rate laws. The functional shape of the measured oxidation ratio $x(t)$ is for all T_{ox} in accordance with the oxidation kinetics for nonlinear field assisted ion diffusion as proposed by Niklasson [19]. On closer inspection, it can be seen that the evolution of the compressive stresses in the Ni phase due to a thermal expansion mismatch $\Delta\alpha$ of Ni and CGO contributes to the enhancement of the oxidation kinetics.

These findings are substantiated by the microstructural analysis of the oxidized samples via FIB cross-sections, which clearly indicate that the oxidation of the Ni cermet is accompanied by the nucleation of Kirkendall voids in

the NiO network. The temperature dependence of the void-size distribution has been proven by void-size analysis from 3-D FIB nanotomography data. The Kirkendall voids formed during oxidation explain the differing activation energy $E_a = 2.8(2)$ eV of the parabolic rate constants k_p from literature data of typically 1.9 eV, as the microstructure of the Ni network changes during oxidation. Experimental evidence is found that the oxidation kinetics of Ni in the Ni/CGO cermet is nonlinear and accompanied by the formation of Kirkendall voids. The nonlinearity of the oxidation kinetics results from the formation a high inbuilt electric field E during oxidation. This high field is related to the compressive stresses evolving because of a thermal expansion mismatch between the constituent materials of the cermet.

For applications where Ni/CGO cermets are used, it has to be considered that once heated over T_{crit}, these materials reach a metastable state with respect to creep and Kirkendall void formation during oxidation. It has been shown that the formation of Kirkendall voids changes irreversibly the microstructure of Ni/CGO cermets during oxidation. This can be interpreted as the onset and main contribution to the long-term degradation caused by redox cycling.

References

[1] Humenik M, Parikh NM. Cermets: I. Fundamental concepts related to micro-structure and physical properties of cermet systems. J Am Ceram Soc 1956;39(2):60–3.

[2] Chan MC, Pakhomov AB, Zhang ZQ. Numerical study of conductance distribution in granular metal films. J Appl Phys 2000;87(3):1584–6.

[3] Leaver KD. The temperature dependence of conductivity in discontinuous thin films and cermets. J Phys C: Solid State Phys 1977;10(2):249.

[4] Miller NC, Hardiman B, Shirn GA. Transport properties, microstructure, and conduction model of cosputtered au sio cermet films. J Appl Phys 1970;41(4):1850–6.

[5] Milner A, Gerber A, Groisman B, Karpovsky M, Gladkikh A. Spin-dependent electronic transport in granular ferromagnets. Phys Rev Lett 1996;76(3):475–8.

[6] Pakhomov AB, Yan X, Zhao B. Giant hall effect in percolating ferromagnetic granular metal-insulator films. Appl Phys Lett 1995;67(23):3497–9.

[7] Permyakov LN, Antonov AA, Isakov VP, Shchetnikova ST. Corrosion failure of a cermet in an oxidizing medium. Atom Energy 1993;75:601–5.

[8] Chien CL. Granular magnetic solids (invited). J Appl Phys 1991;69(8):5267–72.

[9] Takeguchi T, Kikuchi R, Yano T, Eguchi K, Murata K. Effect of precious metal addition to Ni–YSZ cermet on reforming of CH_4 and electrochemical activity as SOFC anode. Catal Today 2003;84(3–4): 217–22.

[10] Shalaev VM, Sarychev AK. Nonlinear optics of random metal-dielectric films. Phys Rev B 1998;57(20):13265–88.

[11] Yokokawa H, Tu H, Iwanschitz B, Mai A. Fundamental mechanisms limiting solid oxide fuel cell durability. J Power Sources 2008;182(2):400–12.

[12] Iwanschitz B, Sfeir J, Mai A, Schütze M. Degradation of SOFC anodes upon redox cycling: a comparison between Ni/YSZ and Ni/CGO. J Electrochem Soc 2010;157(2):B269–78.

[13] Zhang Y, Liu B, Tu B, Dong Y, Cheng M. Understanding of redox behavior of Ni–YSZ cermets. Solid State Ionics 2009;180(36–39): 1580–6.

[14] Sumi H, Kishida R, Kim JY, Muroyama H, Matsui T, Eguchi K. Correlation between microstructural and electrochemical characteristics during redox cycles for Ni–YSZ anode of SOFCs. J Electrochem Soc 2010;157(12):B1747–52.

[15] Busawon AN, Sarantaridis D, Atkinson A. Ni infiltration as a possible solution to the redox problem of SOFC anodes. Electrochem Solid-State Lett 2008;11(10):B186–9.

[16] Fouquet D, Mller A, Weber A, Ivers-Tiffe E. Kinetics of oxidation and reduction of Ni/YSZ cermets. Ionics 2003;9:103–8.

[17] Jeangros Q, Faes A, Wagner J, Hansen T, Aschauer U, herle JV, et al. In situ redox cycle of a nickel-YSZ fuel cell anode in an environmental transmission electron microscope. Acta Mater 2010;58(14):4578–89.

[18] Faes A, Nakajo A, Hessler-Wyser A, Dubois D, Brisse A, Modena S, et al. Redox study of anode-supported solid oxide fuel cell. J Power Sources 2009;193(1):55–64.

[19] Niklasson GA, Karmhag R. Oxidation kinetics of metallic nanoparticles. Surf Sci 2003;532–535:324–7.

[20] Karmhag R, Niklasson GA, Nygren M. Oxidation kinetics of nickel nanoparticles. J Appl Phys 2001;89(5):3012–7.

[21] Atkinson A, Taylor R. The self-diffusion of Ni in NiO and its relevance to the oxidation of Ni. J Mater Sci 1978;13:427–32.

[22] Graham MJ, Cohen M. On the mechanism of low-temperature oxidation (23–450 °C) of polycrystalline nickel. J Electrochem Soc 1972;119(7):879–82.

[23] Karmhag R, Niklasson GA, Nygren M. Oxidation kinetics of small nickel particles. J Appl Phys 1999;85(2):1186–91.

[24] Richard Karmhag Gunnar A, Niklasson MN. Oxidation kinetics of large nickel particles. J Mater Res 1999;14(7):3051–8.

[25] Mrowec S, Grzesik Z. Oxidation of nickel and transport properties of nickel oxide. J Phys Chem Solids 2004;65(10):1651–7.

[26] Atkinson A. Growth of NiO and SiO_2 thin films. Philos Mag B 1987;55:637.

[27] Czerwinski F, Szpunar JA, Macaulay-Newcombe RG, Smeltzer WW. Surface analysis of nickel-oxide films modified by a reactive element. Oxid Met 1995;43:25–57.

[28] Hampikian JM, Potter DI. The effects of yttrium ion implantation on the oxidation of nickel–chromium alloys. I. The microstructures of yttrium implanted nickel–chromium alloys. Oxid Met 1992;38:125–38.

[29] Fromhold AT, Cook EL. Kinetics of oxide film growth on metal crystals: electronic and ionic diffusion in large surface-charge and space-charge fields. Phys Rev 1968;175(3):877–97.

[30] Cabrera N, Mott NF. Theory of the oxidation of metals. Rep Prog Phys 1949;12(163).

[31] Fromhold Jr A. Growth rate of low-space-charge oxides on spherical metal particles. J Phys Chem Solids 1988;49(10):1159–66.

[32] Carter RE. Kinetic model for solid-state reactions. J Chem Phys 1961;34(6):2010–5.

[33] Fromhold AT. Metal oxidation kinetics from the viewpoint of a physicist: the microscopic motion of charged defects through oxides. Langmuir 1987;3(6):886–96.

[34] Thèvenaz P, Ruttimann UE, Unser M. A pyramid approach to subpixel registration based on intensity. IEEE Trans Image Process 1998;7(27).

[35] Kofstad P. Nonstoichiometry, diffusion, and electrical conductivity in binary metal oxides. New York: Wiley; 1972.

[36] Karmhag R, Tesfamichael T, Wckelgrd E, Niklasson GA, Nygren M. Oxidation kinetics of nickel particles: comparison between free particles and particles in an oxide matrix. Solar Energy 2000;68(4):329–33.

[37] Gulbransen EA, Andrew KF. High temperature oxidation of high purity and 1050 nickel between 750. J Electrochem Soc 1957;104(7):451–4.

[38] Kollie TG. Measurement of the thermal-expansion coefficient of nickel from 300 to 1000 K and determination of the power-law constants near the curie temperature. Phys Rev B 1977;16(11):4872–81.

[39] Hayashi H, Kanoh M, Quan CJ, Inaba H, Wang S, Dokiya M, et al. Thermal expansion of Gd-doped ceria and reduced ceria. Solid State Ionics 2000;132(3–4):227–33.

[40] Koning MD. Vacancy-formation thermodynamics in aluminium and nickel: a computational study. Defect Diffus Forum 2003;224–225:59–74.

[41] Zaretsky EB. Impact response of nickel in the 150–1150 K temperature range. J Appl Phys 2009;105(9):093508.

[42] Weinberg K. Void nucleation by vacancy condensation. Proc Appl Math Mech 2008;8(1):10249–50.

[43] Yin Y. Formation of hollow nanocrystals through the nanoscale Kirkendall effect. Science 2004;30(304).

[44] Weinberg K, Bohme T, Muller WH. Kirkendall voids in the intermetallic layers of solder joints in MEMS. Comput Mater Sci 2009;45:827–31.